metals

MDPI

Article

Fracture of $Fe_{95}Ni_5$ Alloys with Gradient-Grained Structure under Uniaxial Tension

Aleksandr Korchuganov *, Dmitrij Kryzhevich and Konstantin Zolnikov

Institute of Strength Physics and Materials Science of Siberian Branch of Russian Academy of Sciences, Akademicheskii 2/4, Tomsk 634055, Russia
* Correspondence: avkor@ispms.ru

Abstract: The fracture behavior of single- (fcc) and two-phase (fcc + bcc) $Fe_{95}Ni_5$ samples with gradient-grained structure, under uniaxial tension, was analyzed via molecular dynamics simulation. The study revealed that fracture initiation and propagation is always associated with grain boundaries. The fracture process develops in three stages. In the first stage, nanopores are formed in the boundaries of coarse grains. The total volume of nanopores at this stage increases slowly due to the formation of new nanopores. The second stage is characterized by a rapid increase in the total nanopore volume due to the formation of nanopores, their growth along the grain boundaries, and their coalescence. At the third stage, the total nanopore volume increases linearly with deformation due to the growth of the largest nanopores. Fracture of two-phase samples begins at higher strains compared to a single-phase sample. With an increase in the volume fraction of bcc lamellae in the original sample, the number of nanopores at the third stage of fracture decreases and tends to one.

Keywords: fracture; crack; phase transition; uniaxial tension; grain boundary; molecular dynamics

Citation: Korchuganov, A.; Kryzhevich, D.; Zolnikov, K. Fracture of $Fe_{95}Ni_5$ Alloys with Gradient-Grained Structure under Uniaxial Tension. *Metals* **2023**, *13*, 1308. https://doi.org/10.3390/met13071308

Academic Editor: Li Liu

Received: 15 June 2023
Revised: 13 July 2023
Accepted: 19 July 2023
Published: 21 July 2023

1. Introduction

The deformation and fracture of nanocrystalline materials depend on many factors. Experimental results have shown that the fracture behavior of these materials can be both ductile and brittle [1]. Some materials with an average grain size of 20 to 100 nm exhibit ductile fracture that occurs via microvoid coalescence [2–5]. Fracture processes in nanocrystalline materials are strongly influenced by the high density of grain boundaries, which are the main sources of nanocrack initiation and growth. This is because the grain boundary regions have an excess atomic volume and weaker atomic bonds in comparison with the grain bulk regions. In ductile fracture induced by nanovoid coalescence, the high diffusivity of grain boundaries contributes to the nanovoid growth. Excess grain boundary energy increases the driving force of intergranular fracture and leads to crack propagation along the grain boundaries. However, the short length of grain boundaries and their curvature at numerous triple junctions significantly restrict intergranular fracture. Intergranular and intragranular fracture processes in nanocrystalline materials strongly compete with each other. They can either proceed simultaneously, or one of them dominates, depending on the loading conditions and structure parameters [1].

The fracture behavior of nanocrystalline materials is also significantly affected by plastic deformation, which has specific features due to nanoscale and interfacial effects. Due to small grain sizes and high grain boundary density, plastic deformation in nanocrystalline materials is characterized by a high-flow stress. Plasticity occurs through lattice dislocation slip and grain boundary mechanisms [6–9]. Lattice dislocation slip is the main plasticity mechanism in nanocrystalline materials with grain sizes ranging from r_c to 100 nm, where r_c is the threshold grain size lying in the range of 10–30 nm for different materials and structures. Full and partial dislocations in the discussed materials are emitted from grain boundaries [10]. Grain boundary deformation mechanisms play the key role in materials with a grain size below the threshold value r_c. Grain boundary mechanisms include grain

boundary sliding, diffusion creep along grain boundaries and triple junctions, and grain rotation [6,7].

Experimental studies have shown that gradient-grained metallic materials have a much higher strength and fracture toughness compared to nanocrystalline materials [11,12]. The physical laws governing the high strength and ductility of gradient-grained metallic materials have been the focus of much research [13–20]. These materials are obtained by either processing of the surface layer or additive manufacturing with controlled growth of the microstructure. In the last two decades, the most widely used techniques for obtaining gradient-grained materials are surface mechanical grinding treatment [21], surface mechanical attrition treatment [14], surface mechanical rolling treatment [22], accumulative roll bonding [23], laser shock peening [24], physical or chemical deposition [25,26], and 3D printing [27]. The grain size in gradient-grained materials increases from the surface to the bulk from several nanometers to micrometers. The motion of dislocations and grain boundary migration play a key role in the deformation behavior of gradient-grained metallic materials and strongly depend on the grain size [28–34]. Experimental studies of a gradient-grained copper film have revealed high values in yield strength and tensile ductility [35]. The high-value characteristics of the film were explained by the mechanically controlled process of grain boundary migration. As a result of deformation incompatibility, the gradient-grained structure converts the applied uniaxial stress to multiaxial stress. This promotes the accumulation and interaction of dislocations and thus contributes to additional strengthening of the material, which is typical of gradient structures and is not observed in materials with a uniform grain size [31].

Computer simulations are widely used to study the deformation mechanisms of gradient-grained metallic materials. It is believed that the relationship between the gradient-grained structure and deformation mechanisms at the microscopic level can be most effectively modeled using the molecular dynamics method [8,9,36–44]. Earlier, we numerically studied the deformation behavior of a gradient-grained FeNi sample under uniaxial tension [8]. The simulations revealed the activation sequence and the degree of contribution of various mechanisms to the sample plasticity. It was found that plasticity in the sample was induced by partial dislocations that form stacking faults in large grains. With further deformation, plasticity is contributed to by trailing, full dislocations and twinning, which gradually affect smaller and smaller grains. Then, intergranular slip and grain boundary migration are activated, and their role in plasticity constantly increases. The evolution of stacking faults was shown to be the main mechanism of plasticity at low strains, while twinning and grain boundary migration dominate at high strains. In [9], we studied the phase transformations, plasticity, and mechanical properties of two-phase $Fe_{95}Ni_5$ (at %) samples with a gradient-grained structure under uniaxial and shear loading. It was found that deformation in the contact region between lamellae and grain boundaries induces the bcc-to-fcc phase transition. By changing the fraction and distribution of the bcc phase in layers with different grain sizes, it is possible to significantly increase the strength of a two-phase, gradient-grained $Fe_{95}Ni_5$ alloy without a substantial decrease in plasticity.

The plastic behavior of gradient-grained materials has been extensively discussed in the literature. Much less attention has been paid to their fracture. In this context, it is interesting to investigate the role of various mechanisms and their interaction on the fracture behavior of gradient-grained materials at the atomic level. This would provide a deeper understanding of the physical processes of fracture and help to design novel materials with improved strength properties.

One of the most common types of failure of metal structures is fatigue failure. As a rule, cracks under cyclic loading initiate and propagate from the surface into the bulk of the specimen. An effective way to prevent surface cracking is to form a gradient-grained structure in the surface layer, which can significantly increase the resistance to fatigue failure in a wide range of cyclic loads [45–48]. In [47], the high fatigue strength of gradient nanograined copper was explained by a synergistic effect from the growth of small grains due to grain boundary migration and the progressive refinement of coarse

grains due to the formation of intragranular dislocation cells. It was found that an increase in the volume fraction of the surface layer with a gradient-grained structure increases the fatigue failure resistance of the whole sample. This is due to the effective inhibition of recrystallization in the nanocrystalline subsurface layer in the direction from the bulk to the surface. The authors of [45,49] revealed that positively graded samples (in which the grain size increases from the surface to the bulk of the material) show better resistance to fatigue crack propagation. In this case, the grain size gradient affects the stress distribution and the size of the plastic zone in the vicinity of the crack tip. The fracture toughness of gradient-grained metallic nickel and its microscopic hardening mechanism were experimentally studied in [49–51].

The complex and highly variable mechanical behavior of materials with different gradient-grained structures is noted in all the above works. The most effective approach to study the fracture of such materials is molecular dynamics simulations. This method is ideal for modeling the fracture process at the atomic level and provides a profound understanding of the complex interaction between various mechanisms responsible for the high-value physical and mechanical properties of gradient-grained materials. A molecular dynamics study of fracture was carried out on nanocrystalline Ni with different grain size gradients [42]. It was found that the crack propagation resistance of the material increases with increasing grain size gradient. This was explained by an increase in fracture toughness due to the growing grain boundary density that prevents crack propagation. Intergranular fracture was observed in samples with a small grain size gradient or uniform grain size. In samples with a large grain size gradient, intergranular cracking becomes transgranular when the crack is arrested by a coarse grain. A further increase in the grain size gradient leads to a greater contribution of transgranular defects to fracture energy dissipation, due to which, the fracture toughness increases. The influence of the grain size gradient on the microstructural evolution of gradient-grained copper samples with an incipient crack in the center was simulated in [43]. It was shown that the higher the grain size gradient, the greater the number of dislocations generated in the crack tip region. Crack propagation in samples with a smaller grain size gradient is suppressed more effectively within the small strain range. At higher strains, a better resistance to fracture is observed in the case of a larger grain size gradient. The behavior of a central crack in a nanocrystalline and gradient-grained copper samples with a uniform grain size under tensile loading was studied via molecular dynamics simulations in [44]. The grain sizes for all samples varied in the range of 5 to 10 nm, which corresponded to the inverse Hall–Petch relation. The simulation results showed that the central crack tends to propagate along oblique, plastic shear bands. In this case, the greatest fracture resistance in gradient-grained samples is provided by finer-grained layers. The cracking resistance also increases with decreasing grain size in nanocrystalline samples. Gradient-grained samples show higher strength only compared to nanocrystalline samples with a larger grain size. The main fracture mechanism for all types of samples is intergranular crack propagation. However, sample size in works [42–44] varied from 1.5 to 2 nm in one direction, which is too small for the plastic deformation mechanisms to work correctly.

The above literature review indicates that further research is needed to more thoroughly investigate fracture processes in gradient-grained metallic materials. Here, we report a molecular dynamics study of the atomic fracture mechanisms of $Fe_{95}Ni_5$ samples with a complex internal structure. Fracture behavior is considered for nanocrystalline fcc and bcc samples with a uniform grain size, and for single- and two-phase gradient-grained samples with different bcc phase fractions under uniaxial tension.

2. Materials and Methods

Molecular dynamics simulations were performed with LAMMPS (version 29Mar19, Sandia National Laboratories, Livermore, CA, USA) [52]. Interatomic interactions in $Fe_{95}Ni_5$ alloy was described by a many-body potential [53] calculated in the framework of an embedded atom method. The potential we used quite correctly describes phase

transitions, stacking fault energies, and elastic moduli in the Fe–Ni system. File with many-body potential [53] in LAMMPS-suitable format is freely available on Interatomic Potentials Repository website [54], which also contains comprehensive information about properties of material calculated using this potential. The Ni atoms were uniformly distributed over the volume of the simulated $Fe_{95}Ni_5$ samples (at %), which had a gradient-grained structure. Layers of the bcc phase in the form of lamellae were generated in fcc grains. For a correct comparison of the results on the relationship between the bcc fraction and fracture behavior, grains in all layers of all simulated gradient-grained $Fe_{95}Ni_5$ samples had the same size, shape, and orientation. The stability of the bcc phase in the Fe–Ni binary system depended both on the Ni content and on the grain size. The simultaneous presence of the fcc and bcc phases in the simulated samples agrees with experimental data [55]. The volume fraction of bcc interlayers in the samples was 0, 30, 50, or 70%. The interlayers were built by cutting each grain along two parallel planes, and the space between the planes was filled with a bcc lattice. The lattice orientation of the bcc and fcc grains satisfied the Nishiyama–Wasserman orientation relationship [56]. The bcc fraction was determined as the quantitative ratio of bcc and fcc atoms. The volume fraction of the bcc phase was set by the thickness of the bcc interlayers and by changing the distance between the parallel cutting planes.

The gradient-grained structure was simulated using the Laguerre–Voronoi tessellation method [57] that implies the partition of space into polyhedral. This method has an advantage over the Voronoi method [58], as it allows precise control of grain sizes when constructing gradient-grained samples. The texture axis of the samples (Y axis in Figure 1) coincided with the [123] crystallographic direction of the fcc lattice. The grains of the sample were rotated along this axis by a random angle so that the angle between adjacent grains was at least 30 degrees.

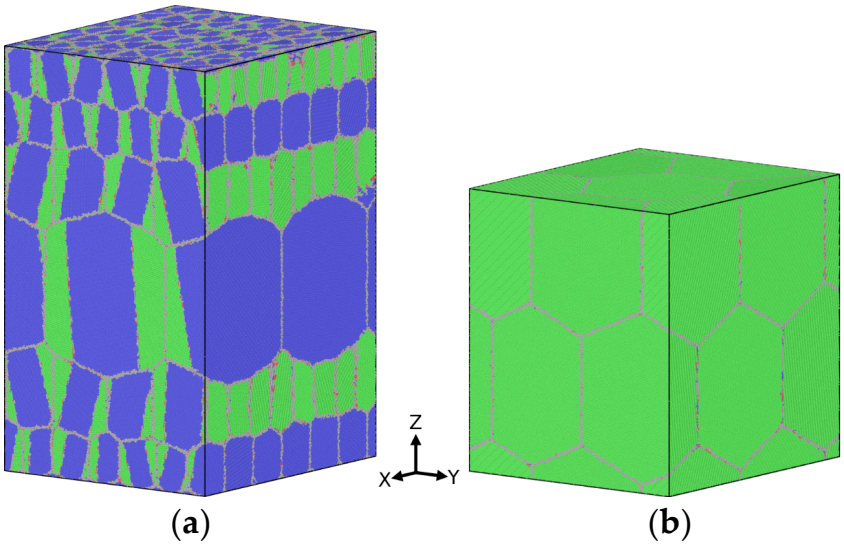

Figure 1. Structure of the simulated gradient-grained sample with 70% bcc fraction (**a**) and a nanocrystalline fcc sample with a grain size of 30 nm (**b**). The fcc and bcc phases are highlighted in green and blue, respectively. The grain boundaries are gray.

The samples were composed of six successive layers oriented along the Z axis with grains of approximately the same size in each layer: small (10 nm), medium (15 nm), and large (30 nm) (Figure 1). The grain centers in each layer were located at the sites of a conditional triangular lattice. Periodic boundary conditions were simulated in all directions. The dimensions of the samples along the X, Y, and Z axes were 60 × 53 × 90 nm. Uniform uniaxial tension was applied to the samples along the Y axis at a speed of 5 m/s by scaling the atom coordinates and the sample sizes in the Y direction. The room temperature during loading was maintained via a thermostat.

Structural defects in the samples were identified using common neighbor analysis [59], which is based on determining the local lattice symmetry in the vicinity of each atom. Intrinsic stacking faults in the fcc lattice were identified in this algorithm as two adjacent atomic planes containing atoms with hcp nearest neighbor symmetry. Atoms located in dislocation cores, phase interfaces, and grain boundaries were characterized via uncertain nearest neighbor symmetry. The atomic volume of each atom was calculated as the volume of the Voronoi polyhedron of the given atom. The structure of the simulated samples was visualized using the OVITO package (version 3.0, OVITO GmbH, Darmstadt, Germany) [60].

3. Results and Discussion

3.1. Fracture of Single- and Two-Phase Samples with a Gradient-Grained Structure

Comprehensive information about the deformation behavior of the samples can be obtained from the tensile curves shown in Figure 2. One can clearly see that an increase in the bcc volume fraction in the samples leads to considerable changes in the stress–strain curve in the strain range of ~3 to 5%. Let us analyze the physical origin of this material behavior in the single-phase sample. The deformation of the sample up to ~3.0% tensile strain is elastic (Figure 2). Further loading leads to the emission of stacking faults from triple junctions and grain boundaries in the coarse-grained layer. Then, layers with medium and small grain sizes are involved in the defect emission process, which is accompanied by the appearance of short, flat portions and a lower slope in the curve. At ~6.50% tensile strain, the first nanopore is formed in the sample in the coarse grain boundary region. At the beginning of fracture, nanopores are formed only at the boundaries of large grains and their junctions (Figure 3). The figure clearly demonstrates that nanopores are formed in the grain boundary and triple junction regions from which stacking faults are emitted. It should be noted that the fracture of the sample throughout the entire stage of deformation is exclusively intergranular. The typical process of nanopore formation and propagation along the boundaries of large and medium grains in the strain range from 8.50 to 9.50% is shown in Figures 3 and 4.

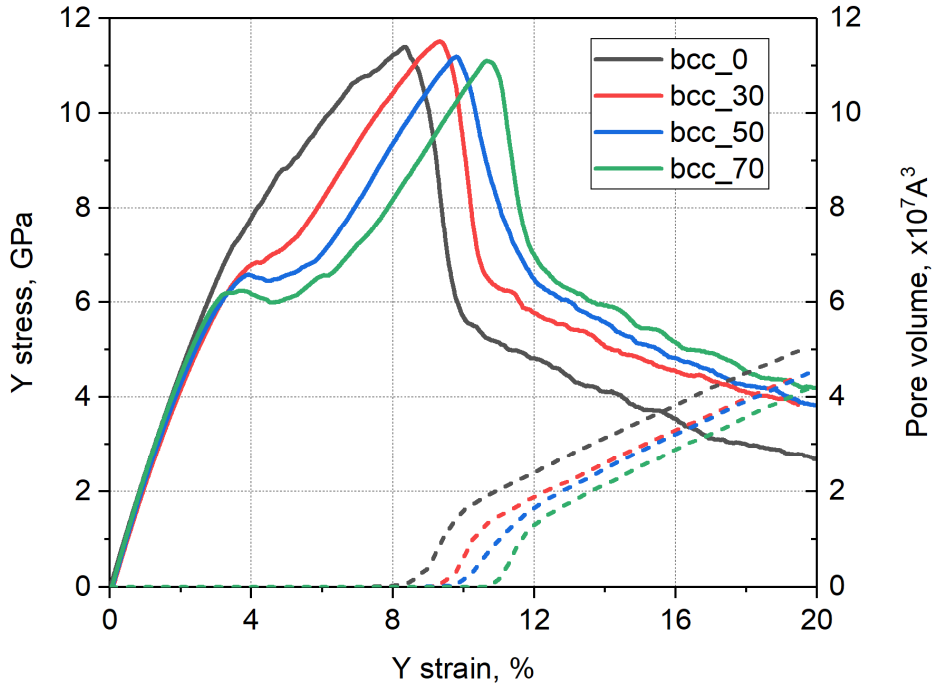

Figure 2. Variation of stress (solid lines) and total nanopore volume (dashed lines) versus strain for samples with different fractions of the bcc phase.

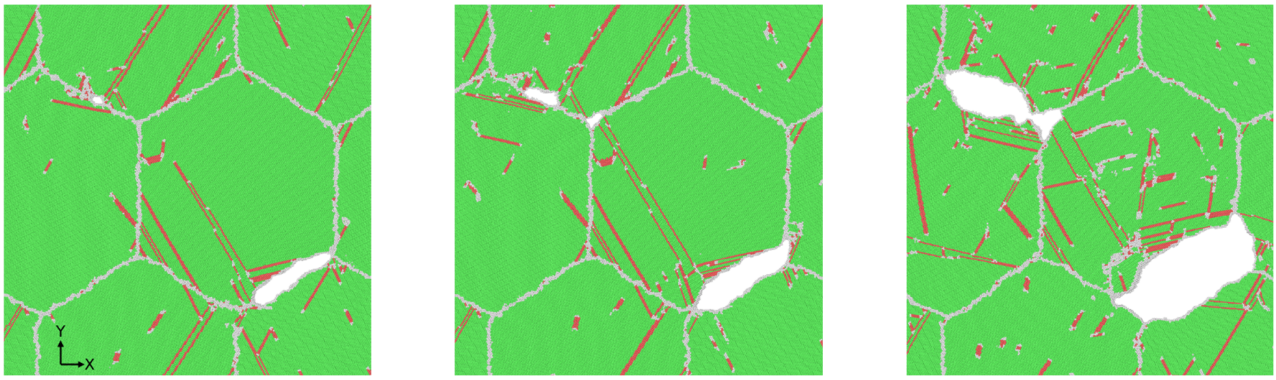

(**a**) (**b**) (**c**)

Figure 3. Nanopores in the coarse-grained layer with a thickness of four lattice parameters perpendicular to the Z axis in the single-phase sample at strains: 8.50 (**a**), 8.75 (**b**) and 9.50% (**c**). Green, red and gray colors denote atoms with fcc, hcp (stacking faults, twins) and uncertain (grain boundaries, free surfaces, dislocations) nearest neighbor symmetry, respectively.

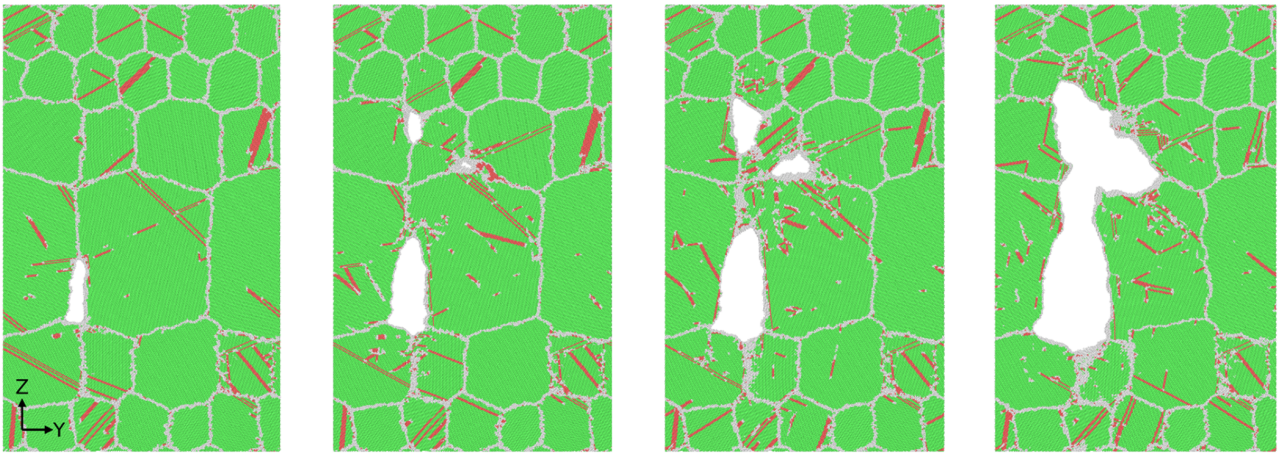

(**a**) (**b**) (**c**) (**d**)

Figure 4. Nanopores in a layer perpendicular to the X axis in the single-phase sample at strains: 8.50 (**a**), 9.00 (**b**), 9.25 (**c**) and 10.00% (**d**). Green, red and gray colors denote atoms with fcc, hcp (stacking faults, twins) and uncertain (grain boundaries, free surfaces, dislocations) nearest neighbor symmetry, respectively.

As follows from Figure 2, the total change in the nanopore volume in the single-phase, gradient-grained sample can be conventionally divided into three stages. At the first stage, when the sample is stretched in the range of 6.50 to 8.50%, the total volume of nanopores increases very slowly. In this case, nanopores are generated only in the coarse-grained layer. At the second stage, in the strain range from ~8.50 to 9.50%, the total nanopore volume rapidly increases, causing an abrupt stress drop in the sample (Figure 2). The total nanopore volume at this stage increases both due to the formation of new nanopores in layers with medium and large grains, and due to the growth of previously formed nanopores. At the third stage with strains above 9.50%, the formation of new nanopores nearly stops, and the main contribution to fracture comes from the growth and coalescence of only a few nanopores. The total nanopore volume at this stage increases linearly with strain. Changes in the variation of the total nanopore volume correlate well with the stress–strain curve behavior in Figure 2.

It should be noted that the strain-induced variation dynamics of the nanopore volume in layers with different grain sizes differs significantly (Figure 5). The coarse-grained layer in the figure is located in the Z coordinate range from 25 to 55 nm. The medium-grained

layers lie in the ranges of 10 to 25 nm and from 55 to 70 nm. All other regions of the sample with the Z coordinate are filled with the fine-grained layers. The grains of each size occupy the same volume of the simulated sample. It can clearly be seen from Figure 5 that the fine-grained layers have good fracture resistance up to a strain of ~9.00%. At higher strains, the contribution of the fine-grained layers to the total volume of nanopores becomes prominent.

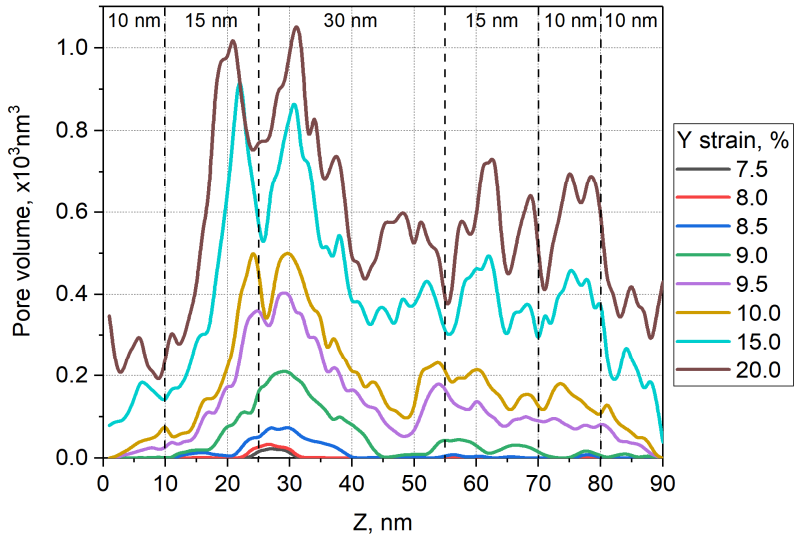

Figure 5. Pore volume distribution along the Z axis for different strains in the single-phase sample. Dashed lines divide layers with different grain sizes.

Now let us consider in detail the fracture of the two-phase Fe95Ni05 alloy under uniaxial tension in a sample containing 70% of the bcc phase. The stress–strain curve of this sample has a more pronounced plateau in the tensile range from 3 to 6%, which begins at lower strains and is characterized by lower stresses compared to other two-phase samples (Figure 2). The elastic behavior of the sample terminates when it is stretched by ~3%. Further stretching gives rise to plastic deformation in the sample, which occurs through the transformation of the bcc lamellae into the fcc phase. The mechanisms of this transformation are described in detail in [9]. The fraction of the bcc phase along the grain size gradient direction at different tensile strains is shown in Figure 6. It can be seen that at ~7.50% strain, the initial bcc lattice in all coarse-grained lamellae transforms into fcc.

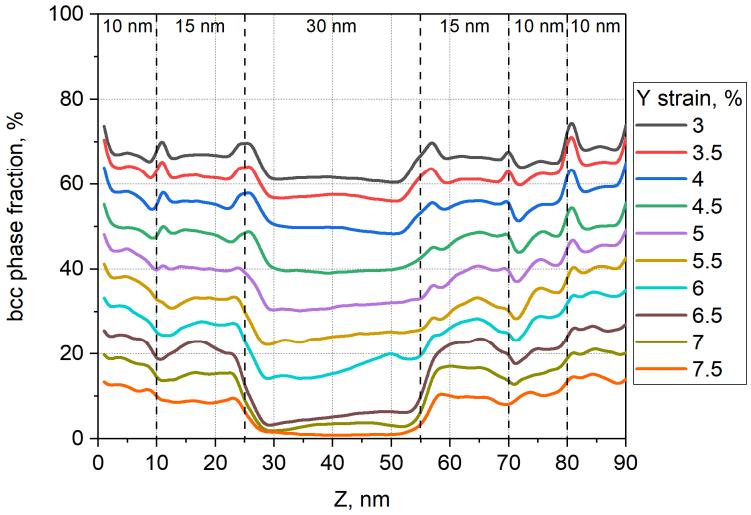

Figure 6. Volume fraction distribution of the bcc phase along the Z axis for different strains in the sample with 70% of bcc phase. Dashed lines divide layers with different grain size.

As a result of the phase transition, some large- and medium-sized grains are fragmented (Figure 7). The pore at the boundary of large grains is formed at a strain of ~10.25%. Starting from 10.50% strain, the nanopore begins to grow rapidly and propagates along the boundary of large grains. Above 11.00% strain, it penetrates into the medium-grained layer. The breakdown of the structure due to the nanopore growth is accompanied by a decrease in the stress–strain curve slope (Figure 2). With further stretching, the nanopore in the coarse- and medium-grained layers continues to grow (Figure 7).

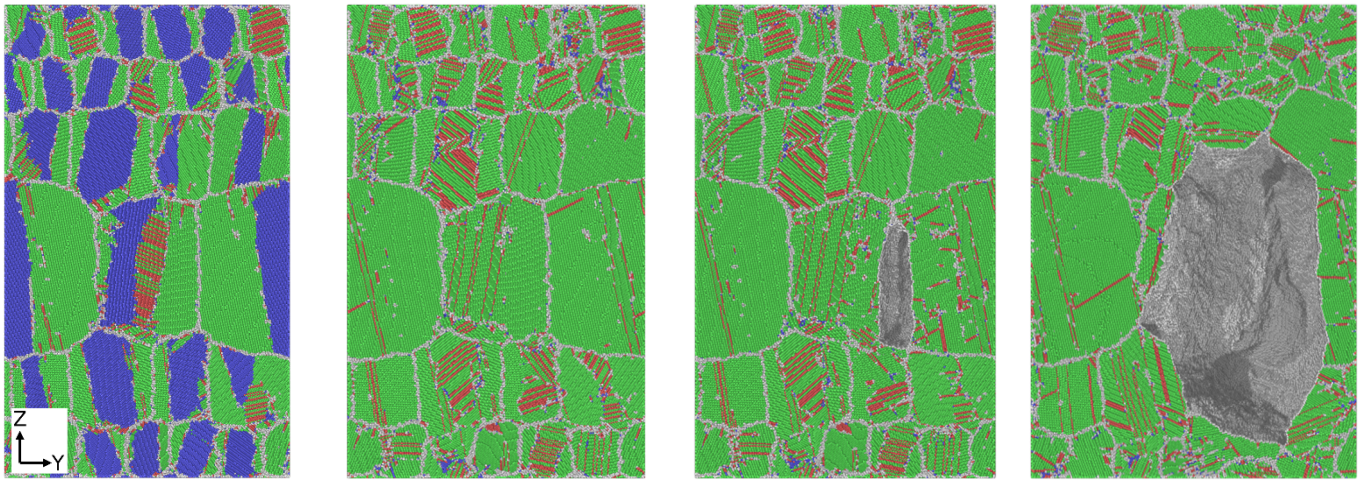

(**a**) (**b**) (**c**) (**d**)

Figure 7. Structure of the two-phase sample with 70% bcc fraction during stretching by: 5.00 (**a**), 10.00 (**b**), 11.00 (**c**) and 20.00% (**d**). Green, red and gray colors denote atoms with fcc, hcp (stacking faults, twins) and uncertain (grain boundaries, free surfaces, dislocations) nearest neighbor symmetry, respectively.

Comparison of the fracture behavior of the simulated samples showed that as the bcc fraction in the original sample increases, fewer nanopores are formed and then grow during stretching. In particular, the number of growing nanopores during fracture was 6, 5, 3, and 1 for single- and two-phase samples with 30, 50, and 70% of the bcc phase, respectively. By comparing the integral stress–strain curves of two-phase samples in Figure 2, it was found that phase transformations begin at lower strain and stress, with a larger fraction of the bcc phase in the lamellae. Since the drop in the stress–strain curves coincides with the beginning of fracture, the increase in the bcc fraction in the original sample enhances the strength of the material.

3.2. Fracture of Nanocrystalline Fcc and Bcc Samples

Fracturing behavior of nanocrystalline $Fe_{95}Ni_5$ samples with fcc and bcc structures under uniaxial tension is qualitatively similar to the behavior of gradient-grained samples. The stress–strain curves of nanocrystalline samples are presented in Figure 8. Analysis of the simulation results showed that an increase in the grain size promotes an earlier formation of nanopores in the studied samples. Fracture in the bcc samples always occurs much later than in the fcc ones. This is because the accommodation of the structure in mechanically loaded bcc samples always starts with the bcc-to-fcc phase transition. This process corresponds to the stress drop after reaching the first peak (green and red curves in Figure 8). The phase transition is more pronounced in the bcc sample with a larger grain size, which leads to a steeper decrease in the stress–strain curve after the first peak. The formation of nanopores in the bcc samples begins only after the bcc-to-fcc phase transformation is completed in all grains. The formation of nanopores in all samples occurs with a rapid stress drop, as evidenced by the correlations of the corresponding curves for stresses and the total nanopore volume in Figure 8. In this case, the higher the strain of the nanopore formation, the higher the growth rate of the total nanopore volume in different

samples. A linear strain dependence of the total nanopore volume always means that nanopores grow due to the coalescence of several largest nanopores or absorption of small nanopores. As in gradient-grained materials, nanopores always nucleate and grow along grain boundaries.

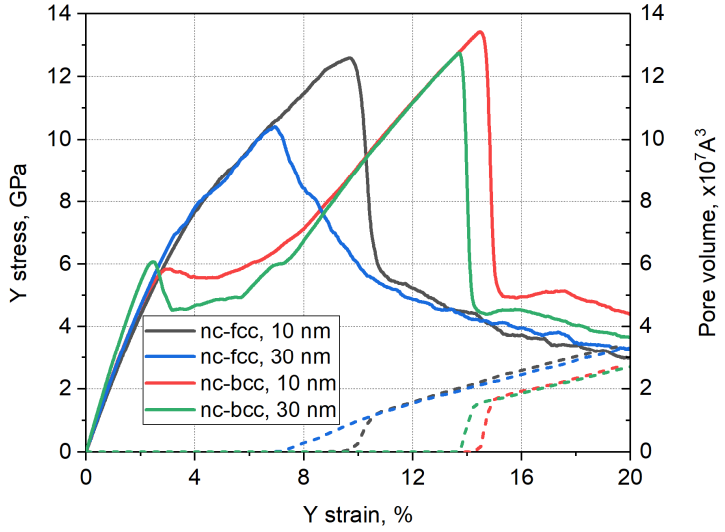

Figure 8. Variation of stress (solid lines) and total nanopore volume (dashed lines) versus strain for nanocrystalline fcc and bcc samples with grain sizes of 10 and 30 nm.

The results obtained are consistent with the experimental data [5] on the fracture behavior of nanocrystalline nickel and Ni-15%Fe alloy under tension. The fracture of pure Ni was shown to occur due to the coalescence of microvoids. Nanocrystalline samples of Ni-15%Fe with an average grain size of about 9 nm failed along the grain boundaries. The main crack was formed through the merging of intergranular nanocracks. Our simulation results are in good agreement with the main findings of the review [1], according to which grain boundaries are the most preferable crack initiation sites in nanocrystalline materials. The molecular dynamics simulations performed in [44] showed that intergranular fracture mechanisms dominate under tension of nanocrystalline copper. The crack propagation resistance increases with decreasing grain size, which is in good agreement with the results of our calculations.

4. Conclusions

The performed simulations have revealed that the fracture process in gradient-grained materials under uniaxial tension can be divided into three stages. The initiation of a fracture is associated with the breaking of interatomic bonds in such materials, and begins in grain boundary regions in the coarse-grained layer. At the first stage of fracture, nanopores begin to form at coarse grain boundaries and triple junctions. The second stage involves both the nucleation of nanopores in grain boundary regions in coarse- and medium-grained layers, and the growth of existing nanopores. The total volume of nanopores at the second stage increases the most rapidly. At the third stage of the fracture, the nanopore volume increases only through the growth of several nanopores and their coalescence. The strain dependence of the total nanopore volume at this stage is linear. The three stages of fracture correlate well with the stress–strain behavior of the samples.

The variation pattern of the total nanopore volume in samples with exactly the same gradient-grained structure but which contain lamellae in the second stage is qualitatively similar to that of single-phase samples. However, the larger the size of lamellae, the later the fracture initiates. Fracture begins only after the structure of almost all lamellae in medium- and large-sized grains transforms into fcc. It was found that the larger the fraction of lamellae in the second stage, the smaller the number of remaining nanopores at the third stage.

Author Contributions: Conceptualization and methodology, A.K. and K.Z.; validation and investigation, A.K. and D.K.; writing—original draft preparation, K.Z.; writing—review and editing, A.K., K.Z. and D.K.; software—D.K.; visualization, A.K. and D.K.; supervision and project administration, A.K. All authors have read and agreed to the published version of the manuscript.

Funding: The study of the deformation behavior of gradient-grained samples was carried out at the financial support of the Russian Science Foundation (Project No. 20-79-10406). The fracture of nanocrystalline fcc and bcc samples was investigated within the Government Statement of Work for ISPMS SB RAS (Project FWRW-2021-0002).

Data Availability Statement: Not applicable.

Conflicts of Interest: The authors declare no conflict of interest.

References

1. Ovid'ko, I.A. Review on the Fracture Processes in Nanocrystalline Materials. *J. Mater. Sci.* **2007**, *42*, 1694–1708. [CrossRef]
2. Kumar, K.S.; Van Swygenhoven, H.; Suresh, S. Mechanical Behavior of Nanocrystalline Metals and Alloys. *Acta Mater.* **2003**, *51*, 5743–5774. [CrossRef]
3. Cheng, S.; Ma, E.; Wang, Y.M.; Kecskes, L.J.; Youssef, K.M.; Koch, C.C.; Trociewitz, U.P.; Han, K. Tensile Properties of in Situ Consolidated Nanocrystalline Cu. *Acta Mater.* **2005**, *53*, 1521–1533. [CrossRef]
4. Youssef, K.M.; Scattergood, R.O.; Murty, K.L.; Horton, J.A.; Koch, C.C. Ultrahigh Strength and High Ductility of Bulk Nanocrystalline Copper. *Appl. Phys. Lett.* **2005**, *87*, 091904. [CrossRef]
5. Li, H.; Ebrahimi, F. Transition of Deformation and Fracture Behaviors in Nanostructured Face-Centered-Cubic Metals. *Appl. Phys. Lett.* **2004**, *84*, 4307–4309. [CrossRef]
6. Wolf, D.; Yamakov, V.; Phillpot, S.R.; Mukherjee, A.; Gleiter, H. Deformation of Nanocrystalline Materials by Molecular-Dynamics Simulation: Relationship to Experiments? *Acta Mater.* **2005**, *53*, 1–40. [CrossRef]
7. Lu, C.; Mai, Y.W.; Shen, Y.G. Recent Advances on Understanding the Origin of Superhardness in Nanocomposite Coatings: A Critical Review. *J. Mater. Sci.* **2006**, *41*, 937–950. [CrossRef]
8. Korchuganov, A.V.; Zolnikov, K.P.; Kryzhevich, D.S. The Contribution of Various Plasticity Mechanisms to the Deformation Behavior of Gradient Nanograined FeNi Alloy. *Metals* **2022**, *12*, 573. [CrossRef]
9. Korchuganov, A.; Kryzhevich, D.; Zolnikov, K. Deformation Behavior of Two-Phase Gradient Nanograined $Fe_{95}Ni_5$ Alloys under Different Types of Loading. *Metals* **2022**, *12*, 1492. [CrossRef]
10. Wu, X.L.; Zhu, Y.T.; Ma, E. Predictions for Partial-Dislocation-Mediated Processes in Nanocrystalline Ni by Generalized Planar Fault Energy Curves: An Experimental Evaluation. *Appl. Phys. Lett.* **2006**, *88*, 121905. [CrossRef]
11. Li, J.; Zhang, Q.; Huang, R.; Li, X.; Gao, H. Towards Understanding the Structure–Property Relationships of Heterogeneous-Structured Materials. *Scr. Mater.* **2020**, *186*, 304–311. [CrossRef]
12. Li, X.; Lu, L.; Li, J.; Zhang, X.; Gao, H. Mechanical Properties and Deformation Mechanisms of Gradient Nanostructured Metals and Alloys. *Nat. Rev. Mater.* **2020**, *5*, 706–723. [CrossRef]
13. Yang, M.; Pan, Y.; Yuan, F.; Zhu, Y.; Wu, X. Back Stress Strengthening and Strain Hardening in Gradient Structure. *Mater. Res. Lett.* **2016**, *4*, 145–151. [CrossRef]
14. Li, J.; Weng, G.J.; Chen, S.; Wu, X. On Strain Hardening Mechanism in Gradient Nanostructures. *Int. J. Plast.* **2017**, *88*, 89–107. [CrossRef]
15. Wang, Q.; Chen, R.; Yang, Y.; Guo, J.; Su, Y.; Ding, H.; Fu, H. Effects of Grain Size and Precipitated Phases on Mechanical Properties in TiAl Gradient Materials. *Mater. Sci. Eng. A* **2018**, *731*, 634–641. [CrossRef]
16. Liu, X.C.; Zhang, H.W.; Lu, K. Strain-Induced Ultrahard and Ultrastable Nanolaminated Structure in Nickel. *Science* **2013**, *342*, 337–340. [CrossRef] [PubMed]
17. Huang, H.W.; Wang, Z.B.; Lu, J.; Lu, K. Fatigue Behaviors of AISI 316L Stainless Steel with a Gradient Nanostructured Surface Layer. *Acta Mater.* **2015**, *87*, 150–160. [CrossRef]
18. An, X.; Bao, W.; Zhang, Z.; Jiang, Z.; Yuan, S.; You, Z.; Zhang, Y. Gradient Enhanced Strain Hardening and Tensile Deformability in a Gradient-Nanostructured Ni Alloy. *Nanomaterials* **2021**, *11*, 2437. [CrossRef]
19. Hasan, M.N.; Liu, Y.F.; An, X.H.; Gu, J.; Song, M.; Cao, Y.; Li, Y.S.; Zhu, Y.T.; Liao, X.Z. Simultaneously Enhancing Strength and Ductility of a High-Entropy Alloy via Gradient Hierarchical Microstructures. *Int. J. Plast.* **2019**, *123*, 178–195. [CrossRef]
20. Lin, Y.; Pan, J.; Zhou, H.F.; Gao, H.J.; Li, Y. Mechanical Properties and Optimal Grain Size Distribution Profile of Gradient Grained Nickel. *Acta Mater.* **2018**, *153*, 279–289. [CrossRef]
21. Liu, X.C.; Zhang, H.W.; Lu, K. Formation of Nano-Laminated Structure in Nickel by Means of Surface Mechanical Grinding Treatment. *Acta Mater.* **2015**, *96*, 24–36. [CrossRef]
22. Xu, W.; Liu, X.C.; Lu, K. Strain-Induced Microstructure Refinement in Pure Al below 100 nm in Size. *Acta Mater.* **2018**, *152*, 138–147. [CrossRef]
23. Zhang, L.; Chen, Z.; Wang, Y.; Ma, G.; Huang, T.; Wu, G.; Jensen, D.J. Fabricating Interstitial-Free Steel with Simultaneous High Strength and Good Ductility with Homogeneous Layer and Lamella Structure. *Scr. Mater.* **2017**, *141*, 111–114. [CrossRef]

24. Ren, X.D.; Zhou, W.F.; Liu, F.F.; Ren, Y.P.; Yuan, S.Q.; Ren, N.F.; Xu, S.D.; Yang, T. Microstructure Evolution and Grain Refinement of Ti-6Al-4V Alloy by Laser Shock Processing. *Appl. Surf. Sci.* **2016**, *363*, 44–49. [CrossRef]
25. Li, J.; Lu, W.; Gibson, J.; Zhang, S.; Chen, T.; Korte-Kerzel, S.; Raabe, D. Eliminating Deformation Incompatibility in Composites by Gradient Nanolayer Architectures. *Sci. Rep.* **2018**, *8*, 16216. [CrossRef]
26. Cheng, Z.; Zhou, H.; Lu, Q.; Gao, H.; Lu, L. Extra Strengthening and Work Hardening in Gradient Nanotwinned Metals. *Science* **2018**, *362*, eaau1925. [CrossRef]
27. Tan, X.; Kok, Y.; Tan, Y.J.; Descoins, M.; Mangelinck, D.; Tor, S.B.; Leong, K.F.; Chua, C.K. Graded Microstructure and Mechanical Properties of Additive Manufactured Ti-6Al-4V via Electron Beam Melting. *Acta Mater.* **2015**, *97*, 1–16. [CrossRef]
28. Zeng, Z.; Li, X.; Xu, D.; Lu, L.; Gao, H.; Zhu, T. Gradient Plasticity in Gradient Nano-Grained Metals. *Extrem. Mech. Lett.* **2016**, *8*, 213–219. [CrossRef]
29. Gao, H.; Huang, Y. Geometrically Necessary Dislocation and Size-Dependent Plasticity. *Scr. Mater.* **2003**, *48*, 113–118. [CrossRef]
30. Zhao, J.; Lu, X.; Yuan, F.; Kan, Q.; Qu, S.; Kang, G.; Zhang, X. Multiple Mechanism Based Constitutive Modeling of Gradient Nanograined Material. *Int. J. Plast.* **2020**, *125*, 314–330. [CrossRef]
31. Wu, X.; Jiang, P.; Chen, L.; Yuan, F.; Zhu, Y.T. Extraordinary Strain Hardening by Gradient Structure. *Proc. Natl. Acad. Sci. USA* **2014**, *111*, 7197–7201. [CrossRef] [PubMed]
32. Li, X.; Wei, Y.; Yang, W.; Gao, H. Competing Grain-Boundary- and Dislocation-Mediated Mechanisms in Plastic Strain Recovery in Nanocrystalline Aluminum. *Proc. Natl. Acad. Sci. USA* **2009**, *106*, 16108–16113. [CrossRef] [PubMed]
33. Hasnaoui, A.; Van Swygenhoven, H.; Derlet, P.M. Dimples on Nanocrystalline Fracture Surfaces as Evidence for Shear Plane Formation. *Science* **2003**, *300*, 1550–1552. [CrossRef]
34. Schäfer, J.; Albe, K. Competing Deformation Mechanisms in Nanocrystalline Metals and Alloys: Coupled Motion versus Grain Boundary Sliding. *Acta Mater.* **2012**, *60*, 6076–6085. [CrossRef]
35. Fang, T.H.; Li, W.L.; Tao, N.R.; Lu, K. Revealing Extraordinary Intrinsic Tensile Plasticity in Gradient Nano-Grained Copper. *Science* **2011**, *331*, 1587–1590. [CrossRef]
36. Fang, Q.; Li, L.; Li, J.; Wu, H. Strengthening Mechanism of Gradient Nanostructured Body-Centred Cubic Iron Film: From Inverse Hall-Petch to Classic Hall-Petch. *Comput. Mater. Sci.* **2018**, *152*, 236–242. [CrossRef]
37. Sun, J.; Ye, H.; Tao, J.; Li, Q.; Zhang, J.; Shen, L.; Zheng, Y.; Zhang, H. Gradient Structure Regulated Plastic Deformation Mechanisms in Polycrystalline Nanotwinned Copper. *J. Phys. D Appl. Phys.* **2019**, *52*, 365304. [CrossRef]
38. Cao, P. The Strongest Size in Gradient Nanograined Metals. *Nano Lett.* **2020**, *20*, 1440–1446. [CrossRef]
39. He, C.Y.; Yang, X.F.; Chen, H.; Zhang, Y.; Yuan, G.J.; Jia, Y.F.; Zhang, X.C. Size-Dependent Deformation Mechanisms in Copper Gradient Nano-Grained Structure: A Molecular Dynamics Simulation. *Mater. Today Commun.* **2022**, *31*, 103198. [CrossRef]
40. Xu, L.; Huang, Z.; Shen, Q.; Chen, F. Atomistic Simulations of Plasticity Heterogeneity in Gradient Nano-Grained FCC Metals. *Mater. Des.* **2022**, *221*, 110929. [CrossRef]
41. Zhou, K.; Zhang, T.; Liu, B.; Yao, Y. Molecular Dynamics Simulations of Tensile Deformation of Gradient Nano-Grained Copper Film. *Comput. Mater. Sci.* **2018**, *142*, 389–394. [CrossRef]
42. Wang, P.; Yang, X.; Tian, X. Fracture Behavior of Precracked Nanocrystalline Materials with Grain Size Gradients. *J. Mater. Res.* **2015**, *30*, 709–716. [CrossRef]
43. Liu, Y.; Yang, F.; Zhang, J. Effects of the Grain Size Gradient on the Microstructural Evolution in Gradient Nano-grained Copper with Initial Central Crack. *Mater. Des. Process. Commun.* **2019**, *2*, e122. [CrossRef]
44. Liu, Y.; Yang, F.; Zhang, X.; Zhang, J.; Zhong, Z. Crack Propagation in Gradient Nano-Grained Metals with Extremely Small Grain Size Based on Molecular Dynamic Simulations. *Int. J. Fract.* **2022**, *233*, 71–83. [CrossRef]
45. Ma, Z.; Liu, J.; Wang, G.; Wang, H.; Wei, Y.; Gao, H. Strength Gradient Enhances Fatigue Resistance of Steels. *Sci. Rep.* **2016**, *6*, 22156. [CrossRef]
46. Long, J.; Pan, Q.; Tao, N.; Dao, M.; Suresh, S.; Lu, L. Improved Fatigue Resistance of Gradient Nanograined Cu. *Acta Mater.* **2019**, *166*, 56–66. [CrossRef]
47. Jing, L.; Pan, Q.; Long, J.; Tao, N.; Lu, L. Effect of Volume Fraction of Gradient Nanograined Layer on High-Cycle Fatigue Behavior of Cu. *Scr. Mater.* **2019**, *161*, 74–77. [CrossRef]
48. Pan, Q.; Lu, L. Improved Fatigue Resistance of Gradient Nanograined Metallic Materials: Suppress Strain Localization and Damage Accumulation. *Scr. Mater.* **2020**, *187*, 301–306. [CrossRef]
49. Wang, Y.; Yuan, L.; Zhang, S.; Sun, C.; Wang, W.; Yang, G.; Li, Q.; Wei, Y. The Influence of Combined Gradient Structure with Residual Stress on Crack-Growth Behavior in Medium Carbon Steel. *Eng. Fract. Mech.* **2019**, *209*, 369–381. [CrossRef]
50. Cao, R.; Yu, Q.; Pan, J.; Lin, Y.; Sweet, A.; Li, Y.; Ritchie, R.O. On the Exceptional Damage-Tolerance of Gradient Metallic Materials. *Mater. Today* **2020**, *32*, 94–107. [CrossRef]
51. Lin, Y.; Yu, Q.; Pan, J.; Duan, F.; Ritchie, R.O.; Li, Y. On the Impact Toughness of Gradient-Structured Metals. *Acta Mater.* **2020**, *193*, 125–137. [CrossRef]
52. Plimpton, S. Fast Parallel Algorithms for Short-Range Molecular Dynamics. *J. Comput. Phys.* **1995**, *117*, 1–19. [CrossRef]
53. Zhou, X.W.; Foster, M.E.; Sills, R.B. An Fe-Ni-Cr Embedded Atom Method Potential for Austenitic and Ferritic Systems. *J. Comput. Chem.* **2018**, *39*, 2420–2431. [CrossRef] [PubMed]
54. Available online: https://www.ctcms.nist.gov/potentials/entry/2018{-}{-}Zhou-X-W-Foster-M-E-Sills-R-B{-}{-}Fe-Ni-Cr/2018{-}{-}Zhou-X-W{-}{-}Fe-Ni-Cr{-}{-}LAMMPS{-}{-}ipr1.html (accessed on 13 July 2023).

55. Wang, H.; Liu, Q.; Zhang, J.; Hsu, T.Y. The Size Effect on the Phase Stability of Nanograined Fe-12Ni Powders and the Magnetic Separation of Face-Centred-Cubic-Body-Centered-Cubic Phases. *Nanotechnology* **2003**, *14*, 696–700. [CrossRef]
56. Nishiyama, Z. X-ray Investigation of the Mechanism of the Transformation from Face Centered Cubic Lattice to Body Centered Cubic. *Sci. Rep. Tohoku Univ.* **1934**, *23*, 637.
57. Hiroshi, I.; Masao, I.; Kazuo, M. Voronoi Diagram in the Laguerre Geometry and Its Applications. *SIAM J. Comput.* **1985**, *14*, 93–105. [CrossRef]
58. Voronoi, G.F. Nouvelles applications des paramètres continus à la théorie de formes quadratiques. *J. Für Die Reine Angew. Math.* **1908**, *134*, 198–287. [CrossRef]
59. Honeycutt, J.D.; Andersen, H.C. Molecular Dynamics Study of Melting and Freezing of Small Lennard-Jones Clusters. *J. Phys. Chem.* **1987**, *91*, 4950–4963. [CrossRef]
60. Stukowski, A. Visualization and Analysis of Atomistic Simulation Data with OVITO-the Open Visualization Tool. *Model. Simul. Mater. Sci. Eng.* **2010**, *18*, 015012. [CrossRef]